Giant Magneto-Impedance (GMI) Magnetometers

Christophe Dolabdjian and David Ménard

Abstract This chapter is about recent advances in giant magneto-impedance (GMI) magnetometer development. The emphasis is put on their performances in terms of equivalent magnetic noise. We first present the physical principles and outline the model of the GMI effect. Next, we establish the relation between the GMI sensing element and the associated electronic conditioning circuits, thus providing expressions for the performances of the device. Our approach is pragmatic and aimed at scientists and engineers concerned with sensitive magnetic measurements. It is hoped that our presentation of the topic will be useful to workers in the field who wish to compare GMI to other magnetic sensors.

1 Introduction

The magneto-impedance (MI) effect refers to the change in the electrical impedance of a ferromagnetic metal due to the application of an external magnetic field. While it was observed and qualitatively understood several decades ago [1], it was not until the development of magnetically ultrasoft metals that the effect was recognized for its potential for magnetic field sensing in the 1990s [2]. By 1994, several groups had reported large impedance variation in CoFeSiB amorphous microwires [3–7] and the term giant magneto-impedance (GMI) was gradually adopted to qualify the effect. In the subsequent years, the effect was observed in a variety of soft magnetic wires and ribbons and the initial phenomenological models were extended into quantitative models. The vast amount of work involved during this first decade of “GMI re-discovery” is too numerous to be properly reported her, but

---

C. Dolabdjian (✉)
Université de Caen Normandie, Caen, France
e-mail: christophe.dolabdjian@unicaen.fr

D. Ménard
Polytechnique Montréal, Montréal, Canada
e-mail: david.menard@polymtl.ca

A. Grosz et al. (eds.), *High Sensitivity Magnetometers*, Smart Sensors, Measurement and Instrumentation 19, DOI 10.1007/978-3-319-34070-8_4

the interested reader may find a comprehensive review of the development over that period in Ref. [8].

Magneto-impedance is a general property of any ferromagnetic metals. However, the effect can be particularly spectacular in ultra-soft magnetic wires and ribbons, whether amorphous or nanocrystalline [8]. The most widely used materials are CoFeSiB-based soft amorphous wires (exact composition varies among different research group). Wires or ribbons can be fabricated, for instance, by in-rotating water quenching [9, see also 10], glass-coated melt spinning [11] and melt extraction [12]. A fairly large number of GMI studies, over the last two decades, have also been dedicated to studies of the effect of various annealing procedures on the GMI response. It is generally accepted that soft amorphous materials with slightly negative magnetostriction coefficient, submitted to a proper stress, current, or combined stress and current annealing, yield the largest GMI ratio and highest sensitivity.

The present chapter is mostly concerned with the exploitation of the GMI effect for the development of magnetic sensors as magnetometers. Section 2 presents the physical basis for modelling the effect. For simplicity, we focus on single domain wires with uniform circumferential anisotropy, thus avoiding any difficulties associated with the details of the domain structure and domain-wall dynamics and of non-uniform anisotropy distribution. While the magnetic susceptibility, and therefore the GMI, can be related to the domain-wall dynamics at low-to-moderate frequencies (such that the domain-wall motion is not damped), we chose to ignore these effects for the following reasons. Domain structures are hard to predict and to control in these ultra-soft magnetic metals, they are most likely a source of magnetic noise, but fortunately they are relatively easy to eliminate, using a small dc bias current, which we usually do in practice.

We also chose not to focus on details of model interpretation, particularly on the confusion or misunderstandings associated with the established link between GMI and ferromagnetic resonance, along with the use of a non-local permeability due to the inclusion of an exchange term in the equation of motion for the magnetization. We will limit ourselves by stating that the non-local permeability, leading to so-called exchange-conductivity effects, have been demonstrated to set fundamental limits on the performance of GMI sensors [13, 14]. The interested reader will find a discussion of these issues in Ref. [15]. Finally, we also chose to limit our discussion to the linear behavior, which leads to simple analytic treatment. A numerical treatment of the non-linear regime has been presented, for instance, in Ref. [16].

In Sect. 3, we are concerned with the sensitivity and noise of an idealized GMI sensor. Contrary to the widespread practice of using the GMI ratio

$$\frac{\Delta Z}{Z} = \frac{Z(B) - Z\left(B_{ref}\right)}{Z\left(B_{ref}\right)}, \tag{1}$$

as a figure of merit, here we adopt the pragmatic point of view that the main criterion relevant to the design of highly sensitive GMI (or low noise GMI) magnetometers is the maximum voltage sensitivity, defined as the derivative of voltage across the GMI sample, at the applied magnetic field at the static working point (bias field) B_0,

$$\left.\frac{\partial V}{\partial B}\right|_{B=B_0}, \tag{2}$$

expressed in V/T. As was recently discussed [17], the GMI ratio is not particularly meaningful as a metric for sensitive magnetometry and it can be misleading in the comparison of the performance between GMI wires from different sources.

Section 4 considers the design of a GMI-based magnetometer, that is, a device which outputs a voltage linearly proportional to the measured field in the full output dynamic range. An overview of the conditioning electronics is presented, along with the estimation of the associated performances. To conclude, the state of art of recent GMI magnetometer development is given.

2 Physics of Magneto-Impedance

2.1 Phenomenology of the MI Effect

Consider a magnetic wire of length l and radius a, driven by a longitudinal electrical current i_{ac} and placed in a longitudinal static magnetic field H_0, as shown in Fig. 1. It is found experimentally that the electrical impedance of the wire depends sensitively upon the longitudinal component of the applied static field. The phenomenon is referred to as magneto-impedance. The complex impedance, $Z = R + iX$, of the wire is obtained from the ratio of the voltage v_{ac} across the wire and the drive current i_{ac},

$$Z = \frac{v_{ac}}{i_{ac}} = \frac{\ell}{2\pi a}\left.\frac{e_z}{h_\varphi}\right|_{surface}, \tag{3}$$

where e_z is the surface longitudinal electric field, and h_φ the circumferential magnetic field. For nonmagnetic conductors, the ratio of the fields on the right hand side of Eq. (3), which corresponds to the surface impedance, is directly calculated from Maxwell's equations. The procedure results in the electrical impedance, which depends on the electromagnetic skin depth.

For magnetic conductors, we may assume a similar dependence of the impedance, provided the classical (non magnetic) skin depth is replaced by an effective skin depth which depends upon the magnetic field. Thus, the normalized impedance will be expressed as

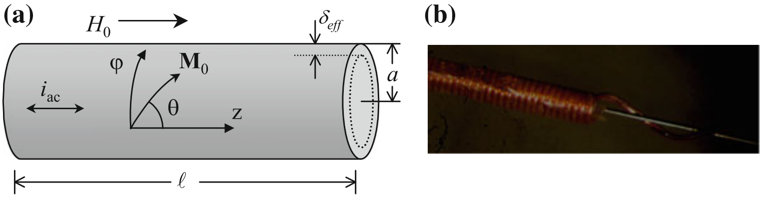

Fig. 1 **a** Ferromagnetic metallic wire driven by an AC current and submitted to a longitudinal magnetic field to be measured. **b** Picture of a wire with an associated coil

$$\frac{Z}{R_{dc}} = \frac{ka}{2}\frac{J_0(ka)}{J_1(ka)}, \tag{4}$$

where R_{dc} is the dc resistance of the wire, and

$$k = \frac{1-i}{\delta_{eff}}, \tag{5}$$

is the radial propagation constant, related to the effective skin depth

$$\delta_{eff} = \sqrt{\frac{2}{\omega\,\sigma\,\mu_{eff}}}. \tag{6}$$

In Eq. (6), ω is the angular frequency, σ is the electrical conductivity, and μ_{eff} is the effective permeability.

In order to observe a strong MI effect, the effective penetration depth, δ_{eff}, of the electromagnetic field must be much smaller than the radius, *a,* of the wire. When this is the case, the ratio of the Bessel functions in the right hand side of Eq. (4) equals the imaginary unit *i*, and Eq. (4) reflects the inverse dependence of the normalized impedance on the effective skin depth

$$\frac{Z}{R_{dc}} = \frac{1+i}{2}\frac{a}{\delta_{eff}}. \tag{7}$$

Equation (7) is generally valid for the GMI response of microwires in the MHz range. However, for frequencies of a few kHz or less, or for sub-micron structures, the situation may be such that the skin depth is much larger than the transverse dimension of the sample. For such cases, the ratio of Bessel functions in the right hand side of Eq. (4) may be expanded in series, which yields

$$Z = R_{dc} + \frac{i\omega\ell}{8\pi}\mu_{eff}. \tag{8}$$

In this limit, we would refer to the effect as magnetoinductive. Since μ_{eff} is generally complex, both the real and imaginary parts of Z may vary appreciably with the field.

The effective permeability, defined by Eqs. (4)–(6), is a useful concept to discuss the physics of the GMI effect. However, it merely displaces the problem from a calculation of the impedance to a calculation of the effective permeability. For the important case of a wire with helical anisotropy, relatively simple, approximate expression for the effective permeability, may be obtained.

2.2 *Effective Permeability*

Consider the cylindrical coordinate system in which the static field H_0 is applied longitudinally along the z-axis, as shown in Fig. 1, with a circumferential easy axis of anisotropy. When there is no applied field, the magnetization is circumferential, that is $\theta = 90°$. Thus, the circumferential component of the dynamic magnetic field produced by the driving current is parallel to the static magnetization. If the drive current is small enough to avoid nonlinear effects, there should be no response from the magnetization, and the material behave as a normal nonmagnetic conductor. Thus, for a circumferential magnetization the effective permeability is trivially μ_0. If the wire is magnetically saturated along the z axis, that is $\theta = 0°$, the coupling between the magnetization and the circumferential field is maximum. This corresponds to a transverse effective permeability which is defined as μ_t. For the general case ($0° \leq \theta \leq 90°$), μ_0 and μ_{t} are related to the diagonal component of the impedance tensor defined in a helical coordinate system with the z' axis at an angle θ from the z axis, that is, parallel to the static magnetization $\mathbf{M}_0$. As an example, for a circumferential uniaxial anisotropy characterized by an energy $K\sin^2\theta$, K is the anisotropy constant (J/m^3), the anisotropy field is given by $H_{\mathrm{k}} = 2\,K/\mu_0 M_{\mathrm{s}}$ and the static equilibrium is given by $\cos\theta = H_0/H_k$. The tensor is then rotated by an angle θ in order to be oriented along the wire axis. The procedure leads to a general effective scalar permeability[1].

$$\mu_{eff} = \left(\sqrt{\mu_t}\cos^2\theta + \sqrt{\mu_0}\sin^2\theta\right)^2. \tag{9}$$

The heart of the problem consists of calculating the transverse effective permeability μ_{t}. Note that, despite the fact that the permeability which enters Maxwell's equations is a 3×3 tensor, the magnetic behavior is effectively determined by a simple scalar effective transverse permeability,

---

[1] See Eq. (49) or Ref. [14]

$$\mu_t/\mu_0 = 1 + m_\varphi/h_\varphi. \tag{10}$$

This follows from the constraint $h_\mathrm{r} = -m_\mathrm{r}$ on the out-of-plane components of the fields, which is a consequence of the dipolar field associated with the radial k-vector, and also from the fact that the components of the fields parallel to the static magnetization do not contribute to the magnetic response. One may alternatively work in terms of a tensor of surface impedance and apply the constraints subsequently, in order to obtain an effective scalar impedance, as was done in Ref. [14].

The effective transverse permeability is calculated from the ferromagnetic torque equation of motion

$$\frac{d\mathbf{M}}{dt} = -|\gamma|\mu_0 \mathbf{M} \times \left(\mathbf{H} + d_{ex}^2 \nabla^2 \mathbf{M}\right) - \mathbf{R}. \tag{11}$$

where $|\gamma|/2\pi$ =28 GHz/T is the gyromagnetic ratio, μ_0 is the permeability of free space, $\mathbf{M}$ is the magnetization vector, and $\mathbf{H}$ is the "Maxwellian" magnetic field, which includes external, dipolar, and demagnetizing fields. While the effective anisotropy field has not been included here for simplicity, it can be easily accounted for, as will be discussed below. The exchange effective field, which arises from non-uniform magnetization vector, is expressed in terms of the exchange length

$$d_{ex} = 2A/\mu_0 M_s^2, \tag{12}$$

where A is the exchange stiffness. In Eq. (11), $\mathbf{R}$ is a phenomenological relaxation term, which can take various mathematical forms, such as a viscous damping (Gilbert term) or a relaxation (modified Bloch-Bloembergen term) or both terms, as

$$\mathbf{R} = \frac{\alpha}{M_s}\mathbf{M} \times \frac{d\mathbf{M}}{dt} + \frac{\mathbf{M} - \mathbf{M}_0}{\tau}, \tag{13}$$

where $\mathbf{M}_0$ is the static part of the magnetization. The Gilbert parameter α is dimensionless and relates to viscous damping, whereas the Bloch-Bloembergen $1/\tau$ term corresponds to a relaxation rate in rad/s. The calculation of the effective permeability from Eq. (11) has been described in detail in previous publications [13, 14].

Let us first consider a wire magnetically saturated in the z direction. Equation (11) is solved in cylindrical coordinates, in a small signal approximation. This leads to a k dependent susceptibility tensor,

$$\begin{pmatrix} m_r \\ m_\varphi \end{pmatrix} = \begin{pmatrix} \chi & -i\kappa \\ i\kappa & \chi \end{pmatrix} \begin{pmatrix} h_r \\ h_\varphi \end{pmatrix}. \tag{14}$$

The tensor components are given by

$$\chi = \frac{\omega_M \tilde{\omega}_H}{\tilde{\omega}_H^2 - \tilde{\omega}^2}, \quad \kappa = \frac{\omega_M \tilde{\omega}}{\tilde{\omega}_H^2 - \tilde{\omega}^2}, \tag{15}$$

where

$$\omega_M = \gamma \mu_0 M_0, \tag{16}$$

$$\tilde{\omega} = \omega - i/\tau, \tag{17}$$

$$\tilde{\omega}_H = \gamma \mu_0 H_0 + i\alpha\omega + \omega_M d_{ex}^2 k^2, \tag{18}$$

are in units of angular frequency. Note the implicit condition $m_z = 0$, which arises from the small signal approximation. Equation (14) describes the response of the dynamic magnetization to an internal dynamic field. The effect of anisotropy and demagnetizing fields, which is neglected here, can be included in Eq. (18) by the replacement of H_0 by an effective internal field. In the *local approximation*, exchange interaction is neglected, and the last term in k^2 is omitted from Eq. (18).

Due to the skin effect, the wave vector k will be perpendicular to the surface of the wire and the fields are expected to vary with the radial coordinate in terms of Bessel functions. Maxwell's equations will then lead to the relations

$$h_r = -m_r, \tag{19}$$

$$h_\varphi = \frac{k_0^2}{k^2 - k_0^2} m_\varphi, \tag{20}$$

where $k_0 = (1 - i)/\delta_0$ relates to the non magnetic skin depth obtained with $\mu_{eff} = \mu_0$ in Eq. (6). With the observation that $k^2/k_0^2 = \mu_{eff}/\mu_0$, Eq. (20) simply restates that $\mu_{eff}/\mu_0 = 1 + m_\varphi/h_\varphi$. The combination of Eqs. (14) and (19) enables one to solve for the scalar transverse permeability

$$\frac{\mu_t}{\mu_0} = 1 + \frac{m_\varphi}{h_\varphi} = \frac{\tilde{\omega}_{AR}^2 - \tilde{\omega}^2}{\tilde{\omega}_R^2 - \tilde{\omega}^2}. \tag{21}$$

where the complex resonance

$$\tilde{\omega}_R^2 = \tilde{\omega}_H(\tilde{\omega}_H + \omega_M), \tag{22}$$

and antiresonance

$$\tilde{\omega}_{AR}^2 = (\tilde{\omega}_H + \omega_M)^2, \tag{23}$$

angular frequencies have been defined for convenience.

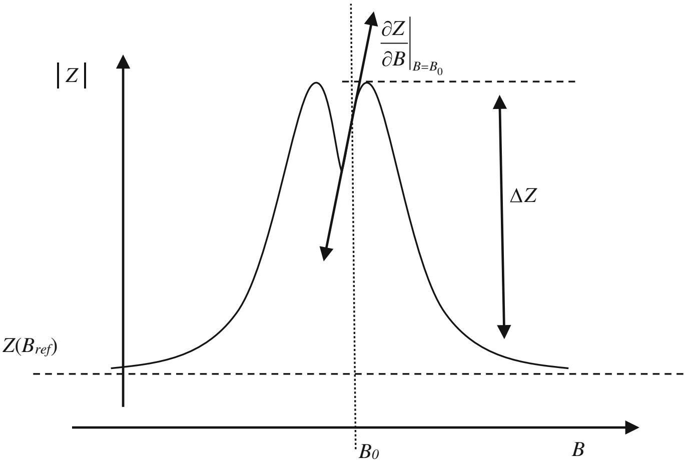

Fig. 2 Characteristic GMI response of a wire as a function of a longitudinal applied field

In the local approximation, Eq. (21) may be substituted directly in Eq. (9), with the proper θ dependence of the effective internal field, which will yield the effective skin depth and thus, the permeability of the wire. Otherwise, the exchange term in Eq. (18) leads to a k-dependent transverse permeability, or equivalently, to spatial dispersion of the permeability. Since μ_t depends on k, which also depends on μ_t, the non-local approach requires a self-consistent solution. Detailed analysis has been presented in Refs. [13, 14].

In summary, combining Eqs. (5), (6), (8) and (20) leads to the normalized impedance

$$\frac{Z}{R_{dc}} = \sqrt{\frac{i\omega\sigma\mu_0 a^2}{4}}\left(\sqrt{\frac{\tilde{\omega}_{AR}^2 - \omega^2}{\tilde{\omega}_R^2 - \omega^2}} + \tan^2[\theta(H_0)]\right)\cos^2[\theta(H_0)]. \tag{24}$$

In Eq. (24), θ is presented as an explicit function of the static external applied field H_0, emphasizing the two mechanisms of impedance variation: magnetization reorientation as a function of the field and field-dependent transverse permeability. Figure 2 illustrates a characteristic GMI impedance variation as the function of a longitudinal applied magnetic, as modeled by Eq. (24). As illustrated, the calculation provides an evaluation of the two figures of merit, defined in Eqs. (1) and (2).

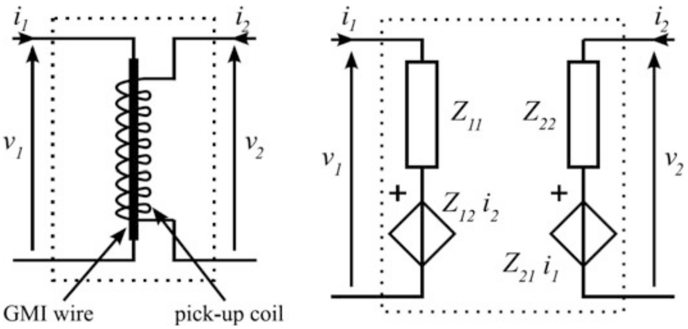

Fig. 3 Sensing element schematic and its associated two port network model illustrating the different terms of the impedance matrix given in Eq. (25) [18]

3 GMI Sensors

3.1 Two-Pole Network Model

Here, we describe how a GMI element can be engineered into a sensor, using a two-port network approach [18]. A schematic of the sensing element is illustrated in Fig. 3, along with the associated two-port network model. It consists of a GMI wire inside a long solenoid or pick-up coil.

The GMI sensing element may be described by its field-dependent impedance matrix $[Z(B_{ext})]$, where $B_{ext} = \mu_0 H_{ext}$ is the longitudinal component of the external magnetic induction.[2] Its expression is

$$\begin{pmatrix} v_1 \\ v_2 \end{pmatrix} = [Z(B_{ext})] \begin{pmatrix} i_1 \\ i_2 \end{pmatrix} = \begin{bmatrix} Z_{11} & Z_{12} \\ Z_{21} & Z_{22} \end{bmatrix} \begin{pmatrix} i_1 \\ i_2 \end{pmatrix}, \tag{25}$$

where v_p and i_p are the voltage across or current into port p (1 or 2), as illustrated in Fig. 3. For operation at low field amplitude in a closed field configuration (feedback loop), the external magnetic induction may be written as

$$B_{ext} = B_0 + b(t), \tag{26}$$

where B_0 is the static working point (bias field) and $b(t)$ is the measured ac signal. Under a small signal approximation, the first order expansion of the impedance components yields

---

[2] Due to strong demagnetizing effect and assuming that we measure fields that are much smaller than the saturation magnetization, the GMI elements are essentially sensitive to the longitudinal component of the field.

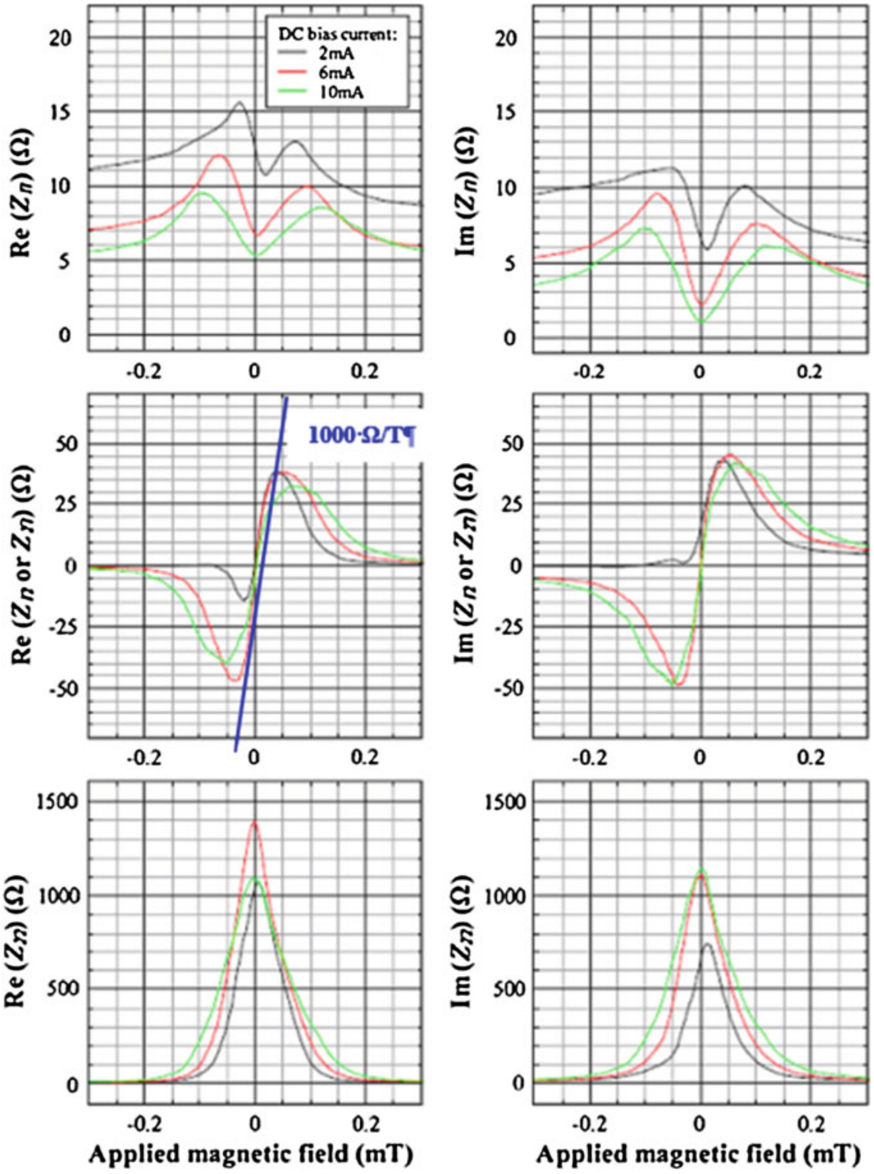

Fig. 4 Real and imaginary parts of the components of the impedance matrix, $Z_{ij}(B)$, as a function of the applied magnetic field for three dc bias currents. Measurements were performed for an excitation frequency, f_0, of 300 kHz. On the Re(Z_{12}) curve, we show an estimated differential variation of the impedance sensitivity, $S_{12-\Omega}$, at a zero field working point in Ω/T [18]

$$Z_{ij} = Z_{ij_0}(B_0) + \left.\frac{\partial Z_{ij}}{\partial B}\right|_{B=B_0} \cdot b(t) = Z_{ij_0} + S_{ij-\Omega} \cdot b(t), \tag{27}$$

where $Z_{ij0} = Z_{ij}(B_0)$ is the impedance at the bias field and $\partial Z_{ij}(B)/\partial B$ ($= S_{ij-\Omega}$) are the intrinsic sensitivity of the corresponding impedance components, in units of Ω/T.

As implied by Eq. (25), there are four different configurations for excitation and detection, each related to a component of the impedance matrix. Examples of measured impedance components, $Z_{ij}(B)$, as a function of applied field are presented in Fig. 4 [18].

The matrix components, in Eq. (25), are given by [19]

$$[Z] = \begin{pmatrix} \frac{l}{2\pi a}\left(Z_M\cos^2\theta_M + Z_N\sin^2\theta_M\right) & N(Z_N - Z_M)\sin\theta_M\cos\theta_M \\ N(Z_N - Z_M)\sin\theta_M\cos\theta_M & \frac{2\pi a N^2}{l_c}\left(Z_M\cos^2\theta_M + Z_N\sin^2\theta_M\right) \end{pmatrix}, \tag{28}$$

where l, l_c, and N are the length of the wire, the length of the pick-up coil, the number of turns of the coil, N, respectively. This expression of the impedance matrix can also be extended to include the parasitic capacitance of the pick-up coil, C_{coil}, yielding [19]

$$[Z'] = \begin{pmatrix} Z_{11} - \frac{jZ_{12}Z_{21}C_{coil}\omega_0}{1 + jZ_{22}C_{coil}\omega_0} & \frac{Z_{12}}{1 + jZ_{22}C_{coil}\omega_0} \\ \frac{Z_{12}}{1 + jZ_{22}C_{coil}\omega_0} & \frac{Z_{22}}{1 + jZ_{22}C_{coil}\omega_0} \end{pmatrix}, \tag{29}$$

where ω_0 is angular frequency of the sinusoidal current excitation of amplitude I_{ac}.

3.2 Sensitivity of the Sensor

The output voltage V_{out} of the sensor, ideally proportional to the measured field, depends upon several factors, including the intrinsic sensitivity, the driving current and the conditioning electronics. Let us consider a typical lock-in detection scheme in any of the four configurations A, B, C or D, as illustrated in Fig. 5. The classical single wire configuration (A configuration), which was treated in Sect. 2, consists of a direct measurement of the wire electrical impedance, whereas the so-called off-diagonal or wire-coil configuration (B configuration), corresponds to an excitation current through the GMI wire, with a voltage detection across the pick-up coil.

The excitation and detection stages consist of a voltage generator, e_{g1}, having an internal resistance, R_1, and associated with carrier compensation circuitry. The detector is a lock-in amplifier, locked to the excitation frequency, f_0 [18]. The output sensitivity, also called the transfer, T_r, at the lock-in amplifier output, expressed in V/T, is defined as

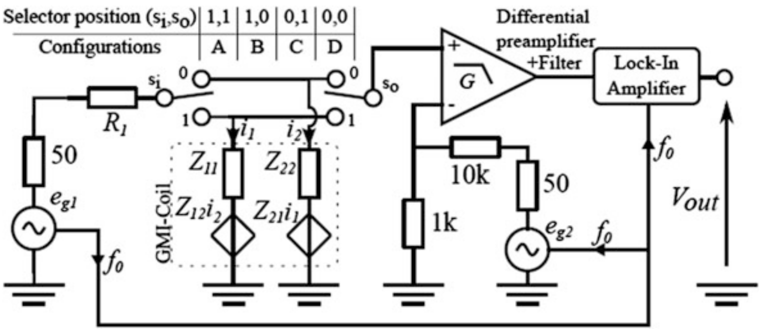

Fig. 5 Diagram of the two-pole network sensor and its associated signal conditioning (preamplifier + detector) [18]

$$T_{rX} = \frac{\partial V_{out}}{\partial B}. \tag{30}$$

where $X = (A, B, C \text{ or } D)$ indicates the measuring configuration and V_{out} is the output voltage. Assuming a linear response, the sensitivity can be obtained from $S_{ij-\Omega}$, Z_{ij0} and the circuit elements. The Fourier transform of the voltage at the lock-in output is given by

$$V_{out}(\omega) \approx G\left[I_{ac}\left(Z_{ij_0}(\omega_0) + \left.\frac{\partial Z_{ij}(\omega_0)}{\partial B}\right|_{B=B_0} \cdot b(\omega) + k_{DS} z_{n_{ij}}(\omega) \right) + k_{DS} e_{n_X}(\omega_0) \right], \tag{31}$$

where G and k_{DS} are the gains associated with the preamplifier and the detector, $z_{n_{ij}}(\omega)$ is the equivalent impedance spectral noise density source, in $\Omega/\sqrt{\mathrm{Hz}}$ and $e_{n_X}(\omega)$ is the equivalent conditioning voltage noise, in $\mathrm{V}/\sqrt{\mathrm{Hz}}$. At the working frequency and the static working point (bias field), the output sensitivity is

$$T_{rX} = G\, I_{ac} \frac{\partial Z_{ij}(\omega_0)}{\partial B} = \frac{I_{ac}}{2} \frac{\partial Z_{ij}(\omega_0)}{\partial B}, \tag{32}$$

and the equivalent voltage noise

$$v_n(\omega) = Gk_{DS} I_{ac}\, z_{n_{ij}}(\omega) + G\, k_{DS}\, e_{n_X}(\omega_0) = \frac{1}{\sqrt{2}}\left[I_{ac}\, z_{n_{ij}}(\omega) + e_{n_X}(\omega_0) \right], \tag{33}$$

where the right hand terms in Eqs. (32) and (33) were obtained by setting $G = 1/2$ and $k_{DS} = \sqrt{2}$, where k_{DS} is a correction factor varying from $\sqrt{2}$ to 1, depending upon the type of synchronous detector or lock-in used [20, 21]. Here, we consider a product detector using a sinusoidal function, at the same frequency and in phase with the carrier.

With an ideal sinusoidal current generator ($R_1 \gg Z_{11}$ or Z_{22}) and a high input preamplifier impedance, the sensitivity of the sensor is simply given by

$$T_{rx} \approx \frac{\partial |Z_{ij}(\omega_0)|}{\partial B} \frac{I_{ac}}{2}. \tag{34}$$

The specifics of electronic conditioning are further discussed below. Details may be found in Ref. [18].

3.3 *Equivalent Magnetic Noise of the Sensor*

3.3.1 Intrinsic Magnetic Noise

It is well known that thermal fluctuations of the magnetization set fundamental limits to the signal-to-noise ratio of magnetic sensors, with a response depending upon the magnetization direction of their sensing elements, with magnetoresistive element as an example [22]. Estimation of the impact of the magnetization fluctuations on the equivalent magnetic noise of GMI sensors was first discussed in [23] and subsequently developed in [24]. More recently, the contribution of the hysteresis losses to the low-frequency noise was considered for the *A* configuration [25] and extended to the *B* configuration in Ref. [26].

Based on the equipartition theorem and a simplified physical model of the GMI response, the intrinsic magnetic noise is expressed by Ménard et al. [23]

$$\overline{z_{n_{ij}}^2(\omega)} \approx \left(\frac{\partial Z_{ij}}{\partial \theta}\right)^2 S_{\theta\theta}^2(\omega) \approx \left(\frac{\partial Z_{ij}}{\partial \theta}\right)^2 \left(\frac{4k_B T \chi''}{2\pi f \mu_0 M_s^2 \vartheta}\right), \tag{35}$$

where $S_{\theta\theta}$ is the spectral density of the magnetization direction fluctuations, χ_t, the magnetic susceptibility, ϑ, the effective volume of the wire, μ_0 the permeability of free space, and $k_B T$, the thermal energy. The imaginary part of the susceptibility, χ'', is related to various dissipation mechanisms. For example, Eq. (35) implies that a viscous damping, proportional to the frequency, yields a frequency independent noise (white noise), whereas frequency independent hysteresis losses, should result in $1/f$ noise at low frequency.

The equivalent magnetic power noise spectral density, in T^2/Hz, is given by the magnetic part of the voltage noise spectral density, Eq. (33), divided by the transfer, Eq. (34), that is

$$\overline{b_n^2(f)} = 2 \frac{\overline{z_{n_{ij}}^2(\omega)}}{\left|\partial Z_{ij}(f_0)/\partial B\right|^2}. \tag{36}$$

In Ref. [27], it was shown that magnetic contribution to white noise is given by

$$\left|\frac{\partial Z_{ij}(f_0)}{\partial B}\right|^2 = \left|\left(-\frac{\sin\theta}{\mu_0 H_{\text{int}}}\right)\frac{\partial Z_{ij}}{\partial \theta}\right|^2. \tag{37}$$

Then, assuming a wire with circumferential anisotropy, the magnetization as a function of field is given by $M/M_s = \cos\theta = H_0/H_k$, and the internal field by $H_{\text{int}} = \left(H_k^2 - H_0^2\right)/H_k$. The sensor is usually operated at a few MHz, with a dc bias field approximately equal to $H_0 = H_k/2$. In these conditions, using Eqs. (35)–(37), an estimate of the equivalent magnetic power noise spectral density, is given by

$$\overline{b_n^2(f)} = \left(\frac{4\mu_0 k_B T \chi''}{\pi f \vartheta}\right)\frac{H_{\text{int}}^2}{|\sin\theta|^2 M_s^2} = \frac{3\mu_0 k_B T}{\pi\vartheta}\frac{H_k^2}{M_s^2}\frac{\chi''}{f}. \tag{38}$$

Assuming a worst case scenario, provided by $\chi'' \approx M_s/H_k$, a very rough estimate of the equivalent magnetic power noise spectral density, in the low frequency regime is

$$\overline{b_n^2(f)} \approx \left(\frac{3\mu_0 k_B T}{\pi\vartheta}\frac{H_k}{M_s}\right)\frac{1}{f}. \tag{39}$$

A lower limit to $1/f$ excess noise, at low frequency, is given by the theoretical intrinsic magnetic white noise, [17]

$$\overline{b_n^2(f)} \approx \frac{Z_{11}^2}{|\partial Z_{11}(f)/\partial B|^2}\left(\frac{4k_B T\alpha}{\gamma\,\mu_0^2 H_K^3 \vartheta}\right), \tag{40}$$

where γ and α are the gyromagnetic ratio and the dimensionless Gilbert damping parameter, respectively. In principle, the Johnson noise of the dc resistance of the GMI sensor, which is included in Eq. (42), should be considered also as an intrinsic noise contribution. In contrast, as discussed below, the white noise regime has been limited so far by the conditioning electronics.

To conclude, the low frequency equivalent magnetic noise spectral density is expected to scale with the impedance sensitivity ratio, with the square root of the absolute temperature, and inversely with the square root of the wire volume. While the analysis above must be considered to be a very rough estimate of the equivalent GMI magnetic noise, numerical values suggest that thermal magnetic noise arising from thermal fluctuations of the magnetization could be a significant contribution to the low frequency intrinsic noise of the sensing element. Further theoretical and experimental studies are required to address this issue in the future.

3.3.2 Noise from the Conditioning Electronics

The output equivalent noise of the system can be estimated based on the classical conditioning circuitry illustrated in Fig. 4. Assuming a well-conditioned electronic circuit, there are three main sources of this noise.

The first is noise induced by the voltage generators, e_g. Signal instability of sinusoidal sources are generally characterized by the single sideband noise spectral density expressed in decibel below the carrier per hertz (dBc/Hz), in direct relation to the output amplitude of the source. This allows one to evaluate the voltage power noise spectral density of the two generators shown in Fig. 4 to be

$$e_{ng_i}^2(f) = \frac{e_{g_i}^2}{10^{\mathrm{dBc}/10+3}} \quad (i = 1, 2), \tag{41}$$

where e_{ng_i} is the amplitude of the sinusoidal signal generator. The order of the dBc, around 100–140 dB at 1 Hz, depends upon the generator performance. The amplitude, e_{g2}, of the second generator is usually related to e_{g1} since the amplitudes of the signals at the inverting and non-inverting inputs of the preamplifier need to be approximately equal. Consequently, the noise level of the second generator, $e_{ng2}(f)$, may be expressed as functions of $e_{ng1}(f)$ and of circuit elements.

The second noise source is that of the preamplifier, which may be summarized by its $(e_n(f) - i_n(f))$ model, considering an input voltage white power $e_{2npreamp}(f)$ and an input current, $i_{2npreamp}(f)$.

The third source is the Johnson noise of each resistor, R, of the setup, including that of the GMI element, expressed as

$$e_{nR}^2 = 4k_B TR, \tag{42}$$

where k_B (1.38×10^{-23} J K^{-1}) is the Boltzmann constant and T (300 °K) is the electronic operating temperature.

Considering an AM signal at the preamplifier input of the form $A_c\,[1 + m\cos(\omega_m t)]\cos(\omega_0 t)$, where ω_m is the angular frequency of the sensed field, $b(t)$, and ω_0 is that of the excitation (driving) current, $I_{ac}(t)$. The filtered demodulated signal is multiplied by $\cos(\omega_0 t)$. Consequently, the output noise spectral density is increased by a factor $G \cdot k_{DS}$, due to the quadratic sum of the noise of the sidebands which have to be considered (cf. Eq. 33). This effectively results in a decrease by a factor k_{DS} of the signal to noise ratio. Consequently, we can express the equivalent output white noise power spectral density given at the output, after demodulation and low-pass filtering, by

$$e_{nx}^2(f) \approx G^2 k_{DS}^2 \left\{ \left(\frac{|Z_{ij_0}(f_0)|}{R_1} \right)^2 \left[2e_{ng1}^2(f) + e_{nR1}^2 \right] + e_{npreamp}^2 + e_{nRx}^2 + R_x^2 i_{npreamp}^2 \right\}. \tag{43}$$

Finally, the equivalent magnetic noise spectral density of the setup, b_{nX}, in pT/√Hz, is defined as the ratio of the electronic noise spectral density (in V/√Hz) to the sensitivity (in V/T), $b_{nX} = e_{nX}/T_{rX}$.

We note that this description leads to a good estimation of the experimental noise and also that the magnetic noise spectral density is dominated either by the excitation or detection stages, depending upon whether the excitation currents, or sensor sensitivity, are high or low. The non-trivial noise behavior exhibited by each configuration (A, B, C, D), leads to a better understanding of the sensor noise limitations. The configuration in which the signal at the coil terminals is measured (often named off-diagonal, $X = B$) appears, at present, to be the most efficient in decreasing the electronic conditioning equivalent output magnetic noise spectral density. Details may be found in Ref. [28].

Overall, the GMI equivalent magnetic noise due to the two main noise source contributions (intrinsic 1/f noise and white conditioning electronic contribution noise) is described by

$$\begin{aligned}\overline{b_{n_X}^2(f)} &\approx \overline{b_n^2(f)} + \overline{e_{n_X}^2(f)}\Big/T_{r_X}^2(f)\\ &\approx 3\mu_0\frac{k_BT}{\pi f\vartheta}\frac{H_K}{M_S} + \frac{k_{DS}^2\Big\{\left(\left|Z_{ij_0}(f_0)\right|/R_1\right)^2\left[2e_{ng1}^2(f)+e_{nR1}^2\right]+e_{npreamp}^2+e_{nRx}^2+R_x^2 i_{npreamp}^2\Big\}}{\left|\partial Z_{ij}(f_0)/\partial B\right|^2 I_{ac}^2}\end{aligned} \tag{44}$$

4 Magnetometer Development

4.1 Conditioning Electronics

There are two principal modes of excitation of a GMI sensor: the classical sine wave generation [18] and pulsed generation [29, 30]. Examples are shown in Figs. 6 and 7. The first provides a single frequency, the second a multiple frequency excitation mode.

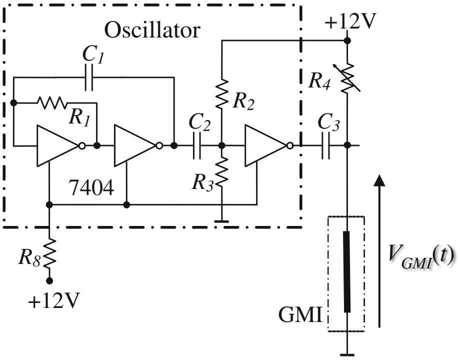

Fig. 6 Typical electronic design based on a pulse generator [31]

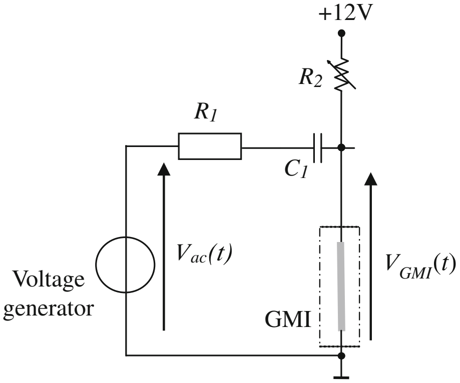

Fig. 7 Typical electronic design based on a sine-wave generator [28]

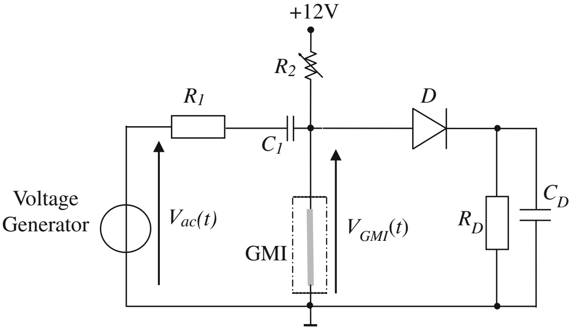

Fig. 8 Classical electronic peak detector associated to a MIG wire as sensor

Based on the Fourier formalism and considering a linear system, both modes are quite similar due to the fact that the first harmonic amplitude dominates for both signals. In both cases, a dc bias current is usually used. This helps to reduce the equivalent magnetic noise of the sensor [31]. There are some other approaches for conditioning electronics, such as a Colpitts oscillator [32], exploiting the GMI wire resonance, but we do not treat them here.

Similarly, there are different types of detectors, such as a peak detector or a lock-in. A typical peak detector is shown in Fig. 8.

4.2 Magnetic Feedback Loop

A GMI magnetometer must exhibit appropriate linearity and magnetic field dynamic range. This can be achieved by using a negative feedback technique, applying a feedback magnetic field. This is applied to the GMI wire via a coil

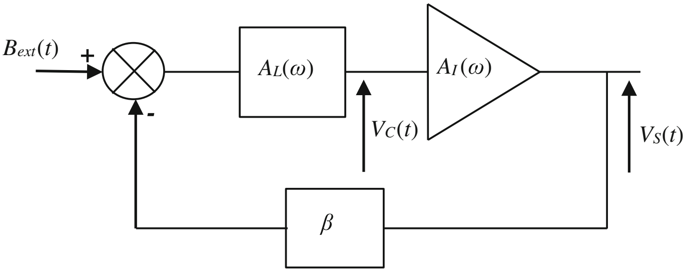

Fig. 9 Sketch view of feedback loop principle

wound around the wire, as illustrated in Fig. 1b. This field locked loop principle is common to several magnetometers. Figure 9 illustrates a typical experimental configuration. The output of the preamplifier, $V_C(t)$, is applied to a low-pass filter, $A_I(\omega)$, to get the magnetometer output signal, $V_S(t)$. The latter is fed back to the GMI coil through a resistor.

Considering a small signal, the system is assumed to be locked on the working point having the highest transfer coefficient T_r ($T_r > 0$). The transfer between the detector and the differential amplifier output is given by

$$A_L(\omega) = \frac{A_L(0)}{1 + j\omega/\omega_L}, \tag{45}$$

where $A_L(0)$ and ω_L are the low frequency gain and cutoff frequency of the amplifier, respectively. Similarly, the transfer function of the low-pass filter is

$$A_I(\omega) = \frac{A_I(0)}{1 + j\omega/\omega_I}, \tag{46}$$

where $A_I(0)$ and ω_I are the low frequency gain and cutoff frequency of the amplifier, respectively. Combining the two, the loop factor of the magnetometer is [33]

$$A(\omega) = T_r\,\beta\,A_L(\omega)A_I(\omega), \tag{47}$$

where β is the ratio of the magnetic flux density applied to the magnetic wire to the feedback current feeding the GMI coil (in units of T/V). Finally, the classical overall small signal transfer function of the magnetometer expresses as a standard second order transfer function is

$$T(\omega) = T_{Mag}\left(\frac{\omega_N^2}{\omega_N^2 - \omega^2 + j\omega\omega_L}\right) \cong \frac{1}{\beta}\left(\frac{\omega_N^2}{\omega_N^2 - \omega^2 + j\omega\omega_L}\right), \tag{48}$$

where $T_{Mag} = \frac{T_r A_I(0) A_L(0)}{1 + T_r \beta A_I(0) A_L(0)} \approx \frac{1}{\beta}$ and $\omega_N^2 = T_r\,\beta A_I(0) A_L(0)\,\omega_I\,\omega_L$.

Let us now consider the large signal behavior of the magnetometer. Around the working point, at which the transfer coefficients are maximal, a rough estimation of the dynamic range available at the pseudo-integrator is [33]

$$-H_{Peak}\ T_r A_L(0) \le V_c(t) \le H_{Peak}\ T_r A_L(0). \tag{49}$$

where $H_{Peak} \approx H_k/2$. It yields that the slew-rate (the maximum rate of change of output voltage per unit of time) at the magnetometer output is limited to

$$\left|\frac{\partial V_S(t)}{\partial t}\right| \approx H_{Peak}\ T_1 A_L(0) A_I(0) \omega_I. \tag{50}$$

This limitation is encountered when a large field step takes place, shifting the magnetic flux density applied to the sensor out of the $\pm H_{peak}$ range. This limitation is quite similar to the large signal response of a locked system. The slew rate limitation also appears for large sinusoidal $B_{ext}(t)$ signals. Further, it requires a low-pass filter time constant, higher than the slew rate. If nothing else in the system saturates, the equivalent magnetic slew rate is deduced from the previous equation to be

$$\left|\frac{\partial B(t)}{\partial t}\right| \approx H_{Peak} T_r \beta A_L(0) A_I(0) \omega_I. \tag{51}$$

In the literature, there are some examples of optimized giant magneto-impedance effect magnetometers [26, 28, 29, 34]. Their performances are in good agreement with the analysis presented here, in terms of equivalent magnetic noise and performance. Table 1 summarizes the state-of-the-art of GMI magnetometer (or sensor) performances.

As an example, the field response model for the sensing element and the noise model are in good agreement with experimental results [26, 28]. Here, the sensing element consists of a thin pick-up coil wound directly on a 100 µm diameter CoFeSiB amorphous ferromagnetic wire (M_s = 561 kA/m, α = 0.02, ρ = 129 µΩ cm). The length of the pick-up coil, l_c, was equal to that of the wire, l, and is about 2.5 cm. The number of turns of the coil, N, is approximately 500 turns/layer. The noise performance of the magnetometer is, approximately, 1.7 pT/$\sqrt{\text{Hz}}$ in the white noise region. It has a bandwidth of about dc-70 kHz, a full scale of 100 µT and a measured slew rate of higher than 450 T/s. A sketch view of the electronic design and the associated equivalent spectral magnetic noise density are shown in Fig. 10.

Table 1 State-of-the-art of GMI sensor or magnetometer performances

Refs.	Mode	Material	Geometry	Current excitation	Excitation frequency (MHz)	Detector	Feed-back loop	Noise level (pT/√Hz)	Bandwidth (Hz)	Dynamic range (μT)
[26, 28]	B	CoFeSiB, 2.5 cm, Ø 30 μm Coil 500 turns	Wire	Sinusoidal	1	Peak detector	Yes	35 @ 1 Hz	100,000	±100
[29]	A	CoFeSiB (1 cm, Ø 30 μm)	Wire	Pulsed	16	Peak detector	Yes	1000 @ 1 Hz	70,000	±25
[32]	B	CoFeNiBSiMo, 1 cm, Ø30 μm Coil 85 turns	Wire	Sinusoidal 2 mA	4	Switch	Yes	10 @ 300 Hz	1000	±250
[34]	B	CoFeSiB, 2 cm, Ø 30 μm Coil 200 turns	Wire	Pulsed	0.4	Switch	No	50 @ 1 Hz	40	±10
[35]	B	$Co_{67}Fe_4Si_8B_{14}Cr_7$ (11 cm × 1 mm × 17 μm) Coil 290 turns (8 cm, Ø 9 mm)	Ribbon	Sinusoidal 10 mA_{rms} 3 mA_{rms}	0.8 0.29	SR840 Analog multiplier	No Yes	17 @ 1 Hz 70 @ 1 Hz	– 10	±1.5 ±75
[36, 37]	D	Fe78Si9B13 (1.2 cm × 2 mm × 20 μm) Coil 100 turns (6 mm)	Ribbon	Pulsed 20 mA	0.3	Peak detector	no	5 kHz	2000	±250
[38]	B	CoFeSiB (1 cm, Ø 30 μm) Coil 600 turns	Wire	Pulsed	0.03	Analog multiplier	no	3 @ 1 Hz	–	>10
[39]	A	Copper path (2 cm × 0.8 mm × 18 μm) under a thin film of CoNbZr (25 × 25mm2 × 4 μm)	Wire	Sinusoidal 20 dBm	600 800	Spectrum analyser No demodulation Phase	No	0.71 @ 500 kHz 1.3 @ 1 Hz		
[40]	A	$Co_{66}Fe_4Si_{15}B_{15}$ (1 cm × 1 mm × 20 μm)	Ribbon	Sinusoidal 10 mA	0.1	Analog multiplier	Yes			±200
[41]	A	$Fe_{75}Si_{15}B_6Cu_1Nb_3$/ Cu/$Fe_{75}Si_{15}B_6Cu_1Nb_3$ [1 cm × 6 cm × (20 μm/40 μm/20 μm)]	Ribbon-multilayer	Sinusoidal	0.16	Lock-in	NO	1000	1000	

(continued)

Table 1 (continued)

Refs.	Mode	Material	Geometry	Current excitation	Excitation frequency (MHz)	Detector	Feed-back loop	Noise level (pT/√Hz)	Bandwidth (Hz)	Dynamic range (μT)
[42, 43]	A	$Fe_{75}Si_{15}B_6Cu_1Nb_3$/ Cu/$Fe_{75}Si_{15}B_6Cu_1Nb_3$ (1 cm × 6 cm × (20 μm/40 μm/20 μm))	Ribbon-multilayer	Sinusoidal	0.6	Lock-in	no	13,000 @ 100 Hz	100	
[44]	B	$Co_{67}Fe_4Si_8B_{14}Cr_7$ (8 cm × 1 mm × 17 μm) Coil 490 turns	Two ribbons	Sinusoidal 1.2 mA_{rms}	0.29	Lock-in	Yes	5.9 @ 1 Hz	15	±75
[45, 46]	A	$Co_{67}Fe_4Mo_{1,5}Si_{16,5}B_{11}$ (3.5 cm × 0.5 mm × 25 μm)	Ribbon	Sinusoidal 10 mA_{rms}	30	Peak detector	yes			±1000
[47]	A	CoNbZr (3 windings - 0.5 cm × 30 μm × 4.3 μm)	Wire	Sinusoidal 40 mA_{rms}	0.37	Spectrum analyser No demodulation	No	1.7 @ 500 kHz		
[48]	B	Co, 2 cm, Ø120 μm Coil 400 turns	Thin film	Sinusoidal	0.4	Lock-in	No	10 @ 2 Hz	5	
[49]	A	Unitika, 4 × 0.3 cm, Ø15 μm	Wire	Sinusoidal	18–30	frequency	yes			±100
[50]	A	$Fe_{4;35}Co_{68,15}Si_{12,15}B_{15}$, 0.3 cm, Ø30 μm	Wire	pulsed	50	peak detector	no		10^6	±100
[51]	A	$[Py/Ti]_3$/Cu/$[Ti/Py]_3$, (2 mm × 130 μm × 590 nm)	μstripe-multilayer	Sinusoidal	120	Peak detector	No	122	100,000	

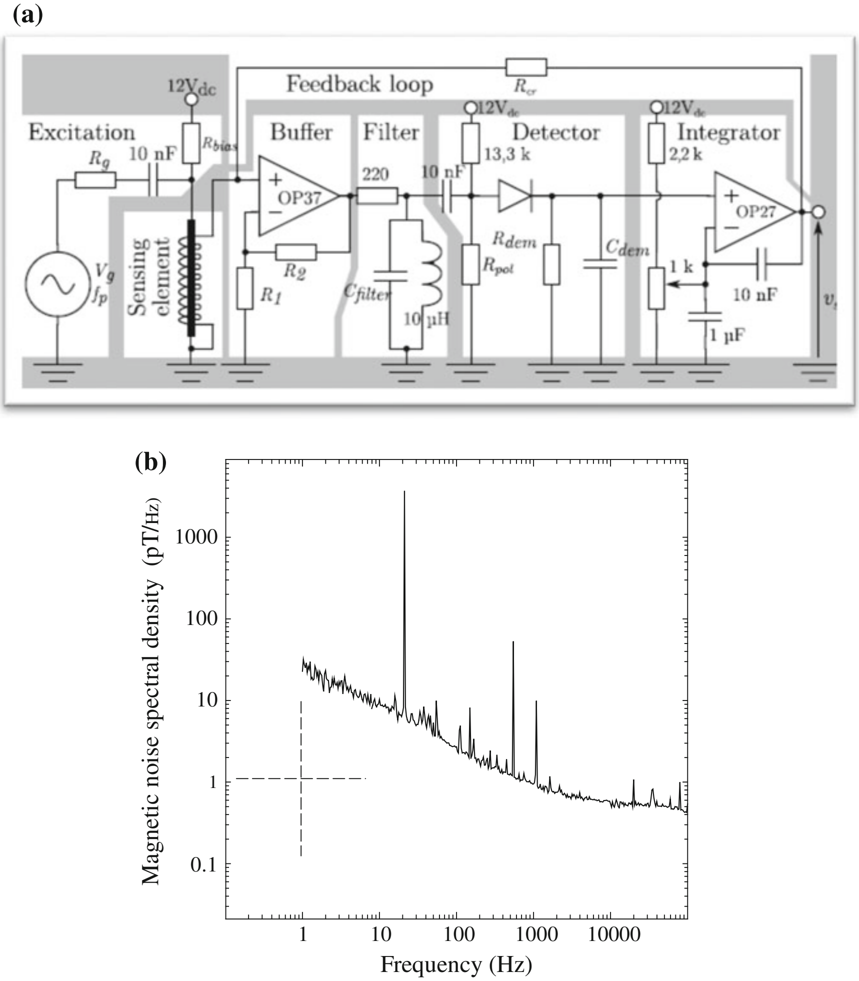

Fig. 10 Sketch view of a full electronic GMI magnetometer design (**a**) and associated equivalent spectral magnetic noise (**b**) [26, 28]

5 Conclusions

While the development of GMI sensor technologies started about two decades ago, advances in the engineering of magnetometers with a systematic evaluation of their noise performances have mostly taken place over the last 10 years. GMI magnetometry in wires, ribbons, single or multi layered films is steadily progressing and is still an active field of research. So far, impressive GMI magnetometer demonstrations have been carried out, exhibiting performances competitive with state-of-the-art low-cost magnetometers operating at room temperature. GMI sensors are also currently considered to be promising candidates for the development of multi-sensor arrays, which could considerably extend their range of applications. Major short-term challenges include the reduction of their low-frequency excess noise and the improvement of their long term magnetic stability. These points have to be addressed, keeping sight of their energy consumption and manufacturing costs, along with other issues pertaining to material studies and optimization.

Acknowledgements We thank Professor Arthur Yelon for his suggestions on the manuscript. Financial support from the Natural Sciences and Engineering Research Council of Canada is gratefully acknowledged.

References

1. E.P. Harrison, G.L. Turney, H. Rowe, Nature **135**, 961 (1935)
2. K. Kawashima, T. Kohzawa, H. Yoshida, K. Mohri. IEEE Trans. Magn. **29**, 3168 (1993)
3. F.L.A. Machado, B.L. da Silva, S.M. Rezende, C.S. Martins, J. Appl. Phys. **75**, 6563 (1994)
4. R.S. Beach, A.E. Berkowitz, Appl. Phys. Lett. **64**, 3652 (1994)
5. L.V. Panina, K. Mohri, Appl. Phys. Lett. **65**, 1189 (1994)
6. V. Rao, F.B. Humphrey, J.L. Costa-Kramer, J. Appl. Phys. **76**, 6204 (1994)
7. J. Velásquez, M. Vázquez, D.-X. Chen, A. Hernando, Phys. Rev. B **50**, 16737 (1994)
8. M. Knobel, M. Vázquez, L. Kraus, in *Handbook of Magnetic Materials*, ed. by K.H. J. Buschow (Elsevier, London, 2003), vol. 15, p. 497
9. T. Masumoto, A. Inoue, M. Hagiwara, US Patent No. 4,523, 626 (1995)
10. I. Ogasawara, S. Ueno, IEEE Trans. Magn. **31**(2), 1219–1223 (1995)
11. H. Chiriac, T.A. Ovari, Prog. Mater Sci. **40**(5), 333–407 (1996)
12. P. Rudkowski, J.O. Ström-Olsen, U.S. Patent 5,003,291 26 March 1991
13. L. Kraus, J. Magn. Magn. Mater. **195**, 764–778 (1999)
14. D. Ménard, A. Yelon, J. Appl. Phys. **88**, 379 (2000)
15. P. Ciureanu, L.-G. Melo, D. Ménard, A. Yelon, J. Appl. Phys. **102**(073908), 1–8 (2007)
16. D. Seddaoui, D. Ménard, B. Movaghar, A. Yelon, J. Appl. Phys. **105**(083916), 1–12 (2009)
17. D. Menard, D. Seddaoui, L.G.C. Melo, A. Yelon, B. Dufay, S. Saez, C. Dolabdjian, Sensor Lett. **7**, 439–442 (2009)
18. B. Dufay, S. Saez, C. Dolabdjian, A. Yelon, D. Menard, IEEE Sens. J. **11**(6), 1317–1324 (2011)
19. B. Dufay, S. Saez, C. Dolabdjian, A. Yelon, D. Menard, IEEE Sens. J. **13**(1), 379–388 (2013)
20. L. Ding, S. Saez, C. Dolabdjian, Sens. Lett. **5**(1), 248–251 (2007)
21. M. Lam Chok Sing, C. Dolabdjian, C. Gunther, D. Bloyet, J. Certenais. Rev. Sci. Instrum. **67** (3), 796–804 (1996)
22. W.F. Egelhoff Jr., P.W.T. Pong, J. Unguris, R.D. McMichael, E.R. Nowak, A.S. Edelstein, J. E. Burnette, G.A. Fischerd, Sens. Actuators, A **155**(2), 217–225 (2009)
23. D. Ménard, G. Rudkowska, L. Clime, P. Ciureanu, S. Saez, C. Dolabdjian, D. Robbes, A. Yelon, Sens. Actuators, A **129**(1–2), 6–9 (2006)
24. L. Melo, D. Menard, A. Yelon, L. Ding, S. Saez, C. Dolabdjian, J. Appl. Phys. **103**(3), 1–6 (2008)
25. C. Dolabdjian, S. Saez, A. Yelon, D. Menard, Key Eng. Mater. **605**, 437–440 (2014)
26. B. Dufay, E. Portalier, S. Saez, C. Dolabdjian, A. Yelon, D. Ménard, *EMSA'14 Conference*, 5–7 July, Vienne (2014)

27. L. Melo, D. Menard, A. Yelon, L. Ding, S. Saez, C. Dolabdjian, J. Appl. Phys. **103**(3), 1–6 (2008)
28. B. Dufay, S. Saez, C. Dolabdjian, A. Yelon, D. Menard, I.E.E.E. Trans, Magn. **49**(1), 85–88 (2013)
29. L. Ding, S. Saez, C. Dolabdjian, L. Melo, D. Menard, A. Yelon, IEEE Sens. J. **9**(2), 159–168 (2009)
30. L. Panina, K. Mohri, Appl. Phys. Lett. **65**(9), 1189–1191 (1994)
31. L. Ding, S. Saez, C. Dolabdjian, P. Ciureanu, L. Melo, D. Ménard, A. Yelon, Sens. Lett. **5**(1), 171–175 (2007)
32. T. Uchiyama, K. Mohri, L.V. Panina, K. Furuno. IEEE Trans. Mag. **31**, 3182–3184 (Nagoya University, Japan) (1995)
33. A. Boukhenoufa, C. Dolabdjian, D. Robbes, IEEE Sens. J. **5**(5), 916–923 (2005)
34. T. Uchiyama, K. Mohri, Y. Honkura, L.V. Panina, IEEE Trans. on Magn. **48**(11), 3833–3839 (2012)
35. M. Malátek, L. Kraus, Sens. Actuators, A **164**(1–2), 41–45 (2010)
36. Y. Geliang, B. Xiongzhu, X. Chao, X. Hong, Sens. Actuators, A **161**(1–2), 72–77 (2010)
37. Y. Geliang, B. Xiongzhu, Y. Bo, L. YunLong, X. Chao, IEEE Sens. J. **11**(10), 2273–2278 (2011)
38. T. Uchiyama, S. Nakayama, K. Mohri, K. Bushida, Physica status solidi (a) **206**(4), 639–643 (2009)
39. S. Yabukami, K. Kato, Y. Ohtomo, T. Ozawa, K.I. Arai, J. Magn. Magn. Mater. **321**, 675–678 (2009)
40. S.S. Yoon, P. Kollu, D.Y. Kim, G.W. Kim, Y. Cha, C.G. Kim, IEEE Trans. Magn. **45**(6), 2727–2729 (2009)
41. F. Alves, L.A. Rached, J. Moutoussamy, C. Coillot, Sens. Actuators, A **142**(2), 459–463 (2008)
42. F. Alves, J. Moutoussamy, C. Coillot, L. Abi Rached, B. Kaviraj, Sens. Actuators, A **145**, 241–244 (2008)
43. F. Alves, B. Kaviraj, L.A. Rached, J. Moutoussamy, C. Coillot, in *Solid-State Sensors, Actuators and Microsystems Conference* (2007). TRANSDUCERS 2007. International, 2581–2584 (2007)
44. L. Kraus, M. Malatek, M. Dvorak, Sens. Actuators, A **142**, 468–473 (2008)
45. M. Kuzminski, K. Nesteruk, H. Lachowicz, Sens. Actuators, A **141**(1), 68–75 (2008)
46. K. Nesteruk, M. Kuzminski, H.K. Lachowicz, Sens. Transduce. Mag. **65**, 515–520 (2006)
47. S. Yabukami, H. Mawatari, N. Horikoshi, Y. Murayama, T. Ozawa, K. Ishiyama, K. Arai, J. Magn. Magn. Mater. **290**, 1318–1321 (2005)
48. E. Paperno, Sens. Actuators, A **116**(3), 405–409 (2004)
49. C.M. Cai, K. Usami, M. Hayashi, K. Mohri, IEEE Trans. Magn. **40**(1), 161–163 (2004)
50. K. Bushida, K. Mohri, T. Uchiyama, IEEE Trans. Magn. **31**, 3134–3136 (1995)
51. E. Fernández, A. García-Arribas, J.M. Barandiaran, A.V. Svalov, G.V. Kurlyandskaya, C. Dolabdjian, IEEE Sensors **15**(11), 6707–6714 (2015)